A numerical study on the effect of cavitation erosion in a Diesel injector

Marco Cristofaro[a,b,*], Wilfried Edelbauer[a], Phoevos Koukouvinis[b], Manolis Gavaises[b]

[a] *AVL List GmbH, Hans–List–Platz 1, 8020 Graz, AT*
[b] *City University London, Northampton Square EC1V 0HB, UK*

Abstract

The consequences of geometry alterations in a Diesel injector caused by cavitation erosion are investigated with numerical simulations. The differences in the results between the nominal design geometry and the eroded one are analyzed for the internal injector flow and spray formation. The flow in the injector is modeled with a 3–phase Eulerian approach using a compressible pressure–based multiphase flow solver. Cavitation is simulated with a non–equilibrium mass transfer rate model based on the simplified form of the Rayleigh–Plesset equation. Slip velocity between the liquid–vapor mixture and the air is included in the model by solving two separate momentum conservation equations. The eroded injector is found to result to a loss in the rate of injection but also lower cavitation volume fraction inside the nozzle. The injected sprays are then simulated with a Lagrangian method considering as initial conditions the predicted flow characteristics at the exit of the nozzle. The obtained results show wider spray dispersion for the eroded injector and shorter spray tip penetration.

Keywords: cavitation erosion; multiphase; Diesel injection; spray

2010 MSC: 00-01, 99-00

Introduction

Cavitation erosion may appear in Diesel injectors at certain operation conditions. A clear trend in Diesel engine designs is to increase the injection pressure to comply stricter norms in terms of emissions. The increase of injection pressure allows to obtain a more efficient combustion process that improves the overall engine efficiency and decreases emissions. At the same time, high injection pressure levels increase the fuel flow velocity inside the injector, leading to local pressure drop that can lead to cavitation. In certain cases, the repetitive vapor cavity collapse may be an aggressive phenomenon that can cause fatigue damages on the nozzle surfaces. The injection operation point selection, and in particular the pressure level, is then a main design trade–off between reducing engine emissions and increasing the risk of incurring in cavitation erosion. Simulation tools that allow to predict the cavitation erosion risk are then of great interest to the injector manufacturers, that could use them in the design process to create geometries less prone to cavitation erosion also at high pressure levels [1, 2, 3].

*Corresponding author
Email address: Marco.Cristofaro@avl.com (Marco Cristofaro)

The prediction of cavitation erosion has been the subject of a wide range of research [4, 5, 6, 7, 8, 9, 10, 11, 12, 13, 14, 15]. Among them, experimental campaigns are of great importance to obtain a deeper understanding of the underlying physics and to allow the validation of numerical models. The very small size of Diesel injector nozzles makes the access to the internal flow very difficult to obtain; thus macroscopic results, such as the flow rate, are usually measured in real size injectors. The detailed flow characteristics can only be quantified with computational fluid dynamics simulations that are validated against measurements obtained in enlarged injectors or simplified real–size nozzles operated at lower pressures [16, 17, 18, 19, 20, 21, 22, 23]. With focus on the cavitation erosion risk assessment, a wide range of empirical models have been developed in the last few years, considering as input the corresponding flow solution results. The main disadvantage of empirical approaches is the introduction of further model hypothesis, whose validity may depend on the specific problem conditions and on the selection of additional tuning parameters. Oppositely, the record of pressure peaks on the wall due to the collapse of vapor cavities does not need to introduce any further hypothesis or tuning parameters. The results are then only dependent on the flow model and their accuracy improves with better resolution and more accurate physics description.

Multi–phase CFD simulations considering flow compressibility are able to capture the pressure waves generated by collapsing vapor clouds and their impact on the nearby surfaces. Density–based solvers were firstly adopted for this purpose. The ability to detect these strong collapsing phenomena and the consequent pressure waves was shown by Sezal et al. in [6] for a micro–channel flow and a 6–hole injectors. They used a density–based solver for the 3–D inviscid Navier–Stokes equations. In [24] Egerer et al. detected also pressure peak values on the same micro–channel flow, but using the single–fluid Large Eddy Simulation (LES) approach. Mihatsch et al. in [11] used a similar solution procedure and conducted a grid dependency analysis of pressure waves intensity. This allowed to define a scaling law in order to fit the simulated pressure peak rates to the one recorded during the experiments. Pressure–based solvers are also able to predict similar high pressure values. Koukouvinis et al. presented in [25] the recorded pressure peaks obtained using a pressure–based solver with a single–fluid LES approach. Results are presented for both a micro–channel flow and a real injector case. Pressure peak intensities of the order of $10,000$ [bar] were recorded. A simplified nozzle geometry was investigated in [26] both experimentally and numerically. Very good agreement of results was found in the vapor volume fraction field (instantaneous and time averaged), which corresponds well with the cavitation erosion locations. The capabilities of a pressure–based solver to fully resolve compressible cavitating flows has been shown in [27] for a simplified throttle flow. The magnitude and importance of slip–velocity between liquid and vapor phase has been assessed. The presence of possibly aggressive cavitation phenomena just after the needle closing has been presented in [28]. These simulations showed complex vapor structures formed due to the sudden flow blockage caused by the needle closing, even for a condition and nozzle geometry

that usually does not exhibit cavitation. The strong correlation between internal nozzle flow and primary spray atomization was shown by various authors in [29, 30, 31, 32]. The location of cavitating vortices inside the nozzle was shown to affect the instantaneous spray pattern.

The main requirement to predict the correct cavitation erosion locations is an accurate description of the cavitating flow. A detailed representation of the physical phenomena involved in the flow can lead to precise erosion predictions thanks to the analyses of the recorded pressure peaks on the walls. The interaction between phase transfer process' and turbulence makes the problem highly computationally demanding and still open to improvements in the numerical methodologies. Furthermore, the magnitude of the recorded pressure peaks is dependent on the numerical model parameters and their exact locations are strongly affected by small flow perturbations; similarly to experimental pitting tests, a long exposure time would then be needed to collect statistically significant data, further increasing the simulation cost.

Most of the studies about cavitation erosion in Diesel injectors aim to identify the aggressiveness of the cavitation phenomena. To the knowledge of the authors, no studies are currently available on the consequences of cavitation erosion with respect to flow field change and spray formation. The present work intends then to investigate the effect of the erosion on the injection system performance. The pressure–based commercial CFD code AVL FIRE™ is used to resolve the multi–phase cavitating flow inside the injector and the spray starting from the nozzle outlet. Implicit time integration is adopted to avoid stability constraints on the simulation time step. The Large Eddy Simulation approach is preferred against Reynolds–Averaged methods in order to resolve the turbulent structures appearing in the flow that are strictly related with cavitation [33]. Even though some authors claim that since cavitation is mainly an inertia driven phenomenon, inviscid equations are sufficient to obtain a correct model [11], in the case of injector flows, very small flow passage gaps exist (e.g. at almost close needle times) along which viscous losses can be non–negligible. Furthermore, recent studies showed that a viscous boundary layer can drastically change the dynamic of a single bubble collapse attached to a wall [34]. Briefly, for the internal nozzle flow the multi–fluid modeling approach is exploited in order to avoid the need of mixture properties definition, instead required for single–fluid approaches. Density and viscosity variation on the wide pressure range has been considered for the fuel liquid phase. Cavitation is included with a mass transfer model between the liquid and vapor fuel phases based on the simplified bubble collapse Rayleigh–Plesset equation. Evaporation and condensation rates are assumed to be caused by the expansion or contraction of a certain number of identical vapor bubbles in each cell. The model is based on the homogeneous mixture assumption of vapor bubbles much smaller than the cell size. A single pressure and velocity is considered to be shared among liquid and vapor and the turbulent kinetic energy of LES is also the same for both phases. The vapor–liquid interface of each bubble is then not resolved and the vapor distribution is described only by the volume fraction. Compared to interface tracking methods, for which each bubble is resolved, this assumption allows to reduce significantly

the resolution requirements and, thus, the computational time. Furthermore, approaches based on the thermodynamic equilibrium hypothesis do not require any bubble modeling assumptions and are expected to have similar computational times to the present approach, however they do not allow the modeling of metastable conditions [35]. To support the current choice we need to refer that even though the assumption that the cell size is larger than the bubble size is not valid in large vapor structures [33], recent studies showed that homogeneous mixture models with very high mass transfer rates converge to the thermodynamic equilibrium model [25, 36]. Then, with a sufficiently high number of bubbles, the thermodynamic states do not deviate excessively from the thermodynamic equilibrium but still allowing metastable conditions. The bubble number density can then be considered as a tuning factor for the relaxation time required for phase change: a higher number density leads to smaller bubbles that reacts faster to local pressure changes. Non–equilibrium models can then be tuned to operate at any condition between non–reacting fluid and instantaneous phase equilibrium. Apart from the simplicity of the model, the application to pressure–based solver is beneficial since it does not need to include special treatments in case negative pressure values are locally reached. The slip velocity between the liquid jet and the air in the combustion chamber is included solving two momentum equations coupled with a droplet's drag model. Pressure peaks are also recorded on wall surfaces and compared with the actual locations of cavitation erosion. Even though the erosion mechanism is still not fully understood, micro jets were visualized only under symmetric vapor distributions and with no external flow velocity; the main cause of cavitation erosion in high speed turbulent flows is then assumed to be caused by shock waves generated by the collapse of interacting vapor cavities. Past studies [35] showed that mesh resolution does not affect significantly the recorded pressure on the wall generated by the collapse of a vapor cloud, thus allowing to assume mesh independent results if the macroscopic vapor structure dynamic is correctly resolved. Following injection, the primary atomization and spray formation are modeled with a Lagrangian particle tracking (LPT) approach suitable for subcritical p–T conditions, where the nozzle outlet flow computed by the internal injector flow simulations has been considered as inlet boundary condition for the spray simulation. Aerodynamic, turbulence and cavitation effects on liquid atomization are considered. As the liquid droplets are injected in the high temperature region, they evaporate creating a fuel vapor cloud.

The present investigation is applied to a Diesel injector used in marine engines with a high–pressure common rail direct fuel injection system. Only the main injection event with a duration of 2.4 [ms] is considered. Experimental visualization showing the erosion area and depth on the injector surfaces are used to generate an eroded geometrical model of the injector. A comparison is carried out between the simulation results for the original and eroded geometry, in terms of internal injector flow and spray. Even though the lack of experiments does not allow to validate the obtained results, this work intends to be an academic study that may trigger future experimental campaigns investigating the effect of material removal due to cavitation on the spray process.

The paper is structured as follows. Initially, a brief description of the numerical model is given, followed by presentation of validation studies. Then further numerical results are presented for the effect of injectors with altered geometry due to erosion on spray formation.

Numerical model

The adopted numerical procedure is different for the in–nozzle flow and the subsequent spray simulations. For the in–nozzle flow, the method is based on the solution of the Navier–Stokes equations describing an iso–thermal compressible 3–phase cavitating flow. In addition to the two fluids coexisting in the domain (liquid fuel and gaseous air), a third gaseous phase is added to model the fuel vapor. In the current approach, a unique pressure is computed for all phases in combination with a multi–fluid approach. Two velocity fields are solved: one for the liquid–vapor mixture and one for the air. Previous studies showed that the slip velocity between vapor and liquid in cavitating flows can be neglected when compared to the main flow velocity [27]. Oppositely, slip velocity between liquid and air in the spray can significantly affect the flow field. The equations are solved iteratively with a pressure–based solver using the Semi–Implicit Method for Pressure–Linked Equations (*SIMPLE*) algorithm [37]. In the present model temperature is fixed in the entire domain and the energy conservation equation is ignored. In the iteration loop the continuity equations are initially solved to compute the volume fraction, α_k, of each phase [1]. In the following step, the two sets of momentum conservation equations are solved. Finally, the common pressure, p, is computed during the pressure correction step and the phase densities, ρ_k, are updated from an appropriate equation of state. The interaction between phases is included in the model by introducing transfer terms in the mass and momentum conservation equations. The mass conservation of each phase is represented by a transport equation with a source term modeling the inter–phase mass transfer, Γ_k. To achieve overall mass conservation, the sum of mass transfer terms over all phases must be zero. Equation 1 shows the mass conservation equation in the differential conservative formulation for the generic phase k.

$$\frac{\partial \alpha_k \rho_k}{\partial t} + \nabla \cdot \alpha_k \rho_k \overline{v}_k = \Gamma_k \tag{1}$$

The volume fraction field of each phase is determined by solving the mass transport equation as in Equation 2. Density, ρ_k^*, and velocity, $\overline{v}_k^*$, are assumed to be known [2].

$$\frac{\partial \alpha_k \rho_k^*}{\partial t} + \nabla \cdot \alpha_k \rho_k^* \overline{v}_k^* = \Gamma_k^* \tag{2}$$

Since the solution of the volume fraction equations are not linked or bounded, the compatibility condition ($\sum_k \alpha_k = 1$) may be *a priori* not satisfied. The obtained volume fraction values are then scaled as shown in Eq. 3.

$$\alpha_k = \alpha_k^* / \sum_k \alpha_k^* \tag{3}$$

Cavitation formation is included in the continuity equations as a mass transfer term between the

[1] The subscript k is used to indicate a quantity related to a generic phase. The letter l is instead used for the liquid phase, v for the vapor phase and g for the gas phase.

[2] The superscript $*$ indicates that the quantity is supposed to be fixed when solving the current equation.

fuel liquid and vapor phases. In the current approach, a model based on a mono–dispersed bubbly flow assumptions is adopted, making use of a simplified version of the Rayleigh–Plesset equation for the single bubble dynamics [16]. The mass transfer term is then obtained by summing the contribution of N identical bubbles to the evaporation and condensation rates as presented in Eq. 4.

$$\Gamma_v = -\Gamma_l = N\,\rho_v\,4\pi R^2\,\dot{R} = \rho_v(3\alpha_v)^{2/3}(4\pi N)^{1/3}\dot{R} \tag{4}$$

The vapor bubble number density is indicated with N, the average bubble radius with R and its rate of change $\dot{R}$. The bubble radius rate of change is derived from the Rayleigh–Plesset equation for a single bubble [38, 39] neglecting thermal, gas content, viscosity and surface tension effects. The bubble radius second order time derivative term is also neglected. The formulation for $\dot{R}$ is then given in Eq. 5.

$$\dot{R} = \pm\sqrt{\frac{2}{3}\frac{|p_{sat}-p|}{\rho_l}} \quad \text{with} \begin{cases} + & \text{if } p \le p_{sat} \\ - & \text{if } p > p_{sat} \end{cases} \tag{5}$$

Pressure values below the saturation pressure, p_{sat}, cause the bubble to expand and thus the liquid phase to evaporate. In this cavitation model, the only tuning parameter is the bubble number density. This value represents the amount of vapor nuclei in the liquid flow and strongly affects the mass transfer rate with which the flow reacts to changes in thermodynamic states across the saturation curve. An infinitely big value of bubble number density leads to infinite mass transfer rates and thus corresponds to thermodynamic equilibrium conditions. In the opposite case, the presence of a few big bubbles causes slow mass transfer flow rates and long relaxation times. Previous studies showed that too small mass transfer rates can lead to physically impossible thermodynamic states: e.g. vapor still existing for pressure values above 100 [bar] [26]. Furthermore, having a fast mass transfer has two beneficial effects on both evaporation and condensation phenomena: reduction of negative pressure (for pressure–based solvers) and increase in the maximum pressure peaks recorded during the cavity collapse. In pressure–based solvers, absolute negative pressure values can appear during the numerical solution of the pressure correction equation [25, 36]. Even though liquids can sustain a certain tension, in case of fast pressure drops very low values are far from the actual thermodynamic state. Since liquids evaporate when the saturation conditions are crossed, the used cavitation model should produce enough vapor to compensate the negative pressure. The vapor formation allows then the fluid to expand, strongly changing its compressibility characteristics and recovering the pressure values to saturation conditions. Since vapor existence is limited to a small range of pressures above the saturation pressure, the mass transfer rate should also be able to transform the vapor back into liquid before too high values of pressure are reached. In cavitation erosive cases, pressure waves are created during the cavity collapse and impact the nearby walls, which can lead to material damage. Fast condensation rates can predict such high values

in pressure at the end phase of cavities collapse [14, 15]; simulations with compressible liquids can predict pressure wave propagation patterns. The maximum pressure peaks can then be recorded on the surfaces and associated with erosion risk. For these reasons, in the current study a purposely high value of 1 [μm^{-3}] is selected for the vapor bubble number density.

In the *SIMPLE* method, a joined mass conservation equation is obtained by combining the mass transport equations of all phases. Considering α_k as known, Eq. 6 is solved to compute the pressure shared among all phases. It is important to notice that due to the division by the phase density, ρ_k, the term Γ_k is not elided, but it is a volumetric flux when phase change occurs and strongly affects the mixture compressibility.

$$\sum_k \frac{1}{\rho_k} \left\{ \frac{\partial \alpha_k^* \rho_k}{\partial t} + \nabla \cdot \alpha_k^* \rho_k \overline{v}_k - \Gamma_k \right\} = 0 \tag{6}$$

It is important to mention that the density scaling is also required to model correctly the system compressibility: the first term of Eq. 6 is elaborated in Eq. 7 [3] considering the single phase speed of sound, defined as $c_k^2 = \partial p / \partial \rho_k$. It should be noted that the sum of the volume fraction time derivatives is zero because derivation is a linear operator and the sum of volume fractions is always 1.

$$\sum_k \frac{\alpha_k}{\rho_k} \frac{\partial \rho_k}{\partial t} = \sum_k \frac{\alpha_k}{\rho_k} \frac{\partial \rho_k}{\partial p} \frac{\partial p}{\partial t} = \left\{ \sum_k \frac{\alpha_k}{\rho_k} \frac{1}{c_k^2} \right\} \frac{\partial p}{\partial t} = \frac{1}{\rho_m c_m^2} \frac{\partial p}{\partial t} \tag{7}$$

The derivation of the mixture speed of sound agrees with Wood's derivation [40].

Subsequently, two momentum conservation equations are solved: one for the liquid–vapor fuel mixture and one for the air. The generic equation is presented in Eq. 8. Momentum transfer and turbulence models provide the closure terms.

$$\frac{\partial \alpha_k \rho_k \overline{v}_k}{\partial t} + \nabla \cdot \alpha_k \rho_k \overline{v}_k \overline{v}_k^T = -\alpha_k \nabla p + \nabla \cdot \alpha_k (\boldsymbol{T}_k + \boldsymbol{T}_k^t) + \overline{M}_k + \overline{v}_i \Gamma_k \tag{8}$$

The vector $\overline{M}_k$ is the inter–phase momentum transfer and $\overline{v}_i$ is the interface velocity. The superscript T indicates the transpose of a vector or a matrix, so that $\overline{v}_k^T$ is a horizontal vector, being $\overline{v}_k$ considered vertical. The term $\overline{v}_i \Gamma_k$ represents the momentum that is carried by the mass transferred between phases. Since no mass transfer exists between liquid–vapor and air and only one equation is solved for the liquid–vapor mixture, this term is not present in both equations. The 3×3 matrix $\boldsymbol{T}_k$ is the shear stress tensor, while $\boldsymbol{T}_k^t$ encloses the effect of the turbulence on the momentum conservation equation. In the present work the Large Eddy Simulation Coherent Structure Model (LES–CSM) is adopted as closure model [41, 33].

The interfacial momentum exchange between liquid–vapor and air is modeled as a drag force caused

[3] The subscript m indicates a quantity computed for a mixture.

by the relative motion of fuel droplets in the air region. The interaction force is then proportional to the relative velocity $\overline{v}_r = \overline{v}_g - \overline{v}_l$. The momentum transfer term can be computed as shown in Eq. 9.

$$\overline{M}_g = -\overline{M}_{lv} = \frac{3}{4} C_D \rho_g \frac{\alpha_{lv}}{D_l} |\overline{v}_r| \overline{v}_r \tag{9}$$

Where D_l is the droplet average diameter set as 0.1 [mm] in the present study. The drag coefficient, C_D, depends on the flow regime around the droplets and it is a function of the droplet Reynolds number, $Re_l = \rho_g |\overline{v}_r| D_l / \mu_g$. The Schiller–Naumann drag model [42] provides an analytical formulation for C_D as shown in Eq. 10.

$$C_D = \begin{cases} \dfrac{24}{Re_l} \left(1 + 0.15 Re_l^{0.687}\right) & Re_l \leq 1,000 \\ 0.438 & Re_l > 1,000 \end{cases} \tag{10}$$

The presented equations are solved in the 3–D domain with the finite volume discretization method. The central differencing second order scheme (CDS) with a 4% blending upwind has been used for the spatial discretization of the momentum conservation equation. The interaction between subgrid–scale (SGS) dissipation and the contribution of the numerical discretization presented by other authors [43, 44] has not been explicitly investigated in this work. Simulation tests were done for fully open needle conditions with both pure CDS and a non–linear differencing scheme (SMART [45]). Results show that even though the average flow does not change significantly, smaller turbulent structures are resolved when the numerical diffusion is reduced by using the pure CDS, leaving a smaller range of the turbulent spectrum to SGS modeling. The overall effect is then that the usage of a second order scheme with less upwind blending reduces both numerical and SGS dissipation. The second order scheme with a 4% blending upwind was then used since it allows to adjust the blending factor accordingly to the simulation stability requirements especially in the deformed cells on the needle seat. To sustain the capabilities of the presented method, a validation for a simple geometry by comparing the velocity profiles extracted from the simulation with experimental measurements was provided in [27]. The good match between velocity profiles can be considered as an indirect validation of the combination of SGS model and adopted numerical discretization method. The continuity equation has been instead discretized with the *MINMOD* scheme [46]. Time integration has been also done with the second order accurate three–time level backward differencing scheme. The convergence of the system of equations is obtained with a *SIMPLE* algorithm, for further details see [47]. Converge criteria of normalized residuals for continuity, momentum and volume fraction equations was set to 10^{-3} and the resulting average number of iterations per time step was of 3. During the needle opening phase at the start of the simulation, up to 50 iterations per time step were needed to reach convergence. One benefit of pressure–based solvers is that the same numerical procedure can be used for both compressible and incompressible simulations. Consequently, a simple switch between compressible and incompressible flow fields simulations can be

obtained, with no major modifications in the numerical algorithm.

In order to exchange the data from the internal nozzle flow to the spray simulation, an ASCII file has been written during the injector flow simulation, which contains all the necessary instantaneous flow variables at the nozzle outlet as presented in [48, 49]. This *nozzle file* contains the time–dependent values of local flow data (velocity components, turbulent kinetic energy and dissipation rate, volume fraction and density) on all $4,700$ orifice faces from which the nozzle outlet is composed in the injector mesh. This approach allows to couple two simulations that are using two very distinct numerical methodologies in a simple manner while maintaining time dependency between the two. Due to the very different space and time resolution the spray simulations computational cost ($\sim$ 200 CPU hours) is 2 orders of magnitude cheaper compared to LES of the internal injector simulations ($\sim 20,000$ CPU hours).

The spray simulations adopted an Eulerian–Lagrangian coupled approach, in which the gas in the system consists of twelve gas species and is modeled by solving Reynolds–Averaged Navier–Stokes (RANS) equations with the k–$\mathcal{E}$ turbulence model, while the liquid droplets are modeled as parcels computed with the Lagrangian approach. Since the spray is a free stream problem, the k–$\mathcal{E}$ turbulence model was selected as one of the most commonly used models in industrial applications, without adding the complexity related to advanced models mainly developed for a more accurate description of boundary layers. Similarly to the numerical model presented for the internal injector flow, the continuity equation, Eq. 6, and the momentum conservation equation, Eq. 8, are solved for the gaseous fraction of the flow. In this model, the closure term for the momentum conservation equation, $\boldsymbol{T}_g^t$, is obtained solving two additional transport equations for the turbulent kinetic energy, k_g, and the turbulent dissipation rate, $\mathcal{E}_g$, as described in [50, 47]. Furthermore the total enthalpy, h_g, conservation equation is solved during the iteration loop to include temperature effects on the spray. The formulation is shown in Eq. 11 and includes the conduction and turbulent heat fluxes, q_g and q_g^t respectively.

$$\frac{\partial \rho_g h_g}{\partial t} + \nabla \cdot \rho_g \overline{v}_g h_g = \nabla \cdot (q_g + q_g^t) + \nabla \cdot (\boldsymbol{T}_g + \boldsymbol{T}_g^t) \cdot \overline{v}_g + \frac{\partial p}{\partial t} \tag{11}$$

For the Lagrangian flow description the differential equation of motion for the liquid droplets parcels is expressed in Eq. 12 [4].

$$\frac{\partial \overline{v}_d}{\partial t} = \frac{3}{4} C_D \frac{\rho_g}{\rho_d} \frac{1}{D_d} |\overline{v}_r| \overline{v}_r \tag{12}$$

The droplet velocity, $\overline{v}_d$, changes due to the drag force, which is the dominant effect on the droplet motion in high pressure injection [47]. The drag force is a function of the density ratio between the gaseous medium and liquid, ρ_g/ρ_d, the droplet diameter, D_d, and the relative velocity between the surrounding flow and the droplet, $\overline{v}_r$. The same formulation as in Eq. 10 is adopted for the drag coefficient. The

[4] The subscript d is used to refer quantity related to the droplets

spray is generated by introducing 200 blobs parcels during each time step randomly sampled within the cross section on the nozzle outlet. Each parcel is initialized with the local velocity and turbulence level at the corresponding time and location of the internal injector simulations, that are stored in the nozzle file. In order to have a consistent injected mass between nozzle flow and spray simulations, the number of blobs contained in each parcel is based on the injected mass during the current time step. The blobs diameter is instead assumed to be the same as the nozzle outlet. The primary atomization model generates droplets from the blobs by considering the competing effects of turbulence and aerodynamically induced break–up processes. Vapor volume fraction distribution though the nozzle out is considered with the effect of bubbles collapsing outside the nozzle as enhancement phenomenon of turbulence induced break–up. Detailed description of the method is available in [51, 47]. Further downstream along the spray, the size of the droplets are affected by two main phenomena: evaporation, modeled as described by Abramzon and Sirignano [52] and secondary break–up, modeled with the WAVE model [53].

Geometrical model and simulation set–up

Computational Mesh. One out the 9 holes of a Diesel injector corresponding to a 40° slice has been modeled. The computational domain starts from 7 [mm] above the needle seat, corresponding to a $L/D_h = 7$, being D_h the hydraulic diameter in the corresponding flow region. The nozzle hole length is 1.1 [mm] and the hole inlet and outlet diameter, D_n, are respectively of 0.22 and 0.21 [mm]. The nozzle inlet is rounded on the upper side with a radius of 75 [μm]. A discharge volume is also included to model the spray region with a length of 8 [mm], corresponding to a $L/D_n = 37.2$. The main geometry dimensions are presented in Fig. 1. The needle movement is modeled by stretching the needle seat region cells. The mesh is formed by structured blocks composed of hexahedral cells. Large Eddy Simulation requirements prescribe a certain cell size in order to be able to resolve the turbulence inertial sub–range and model only the dissipative scales that satisfy the isotropic hypothesis. The cell size inside the channel should then be of the order of 10 times the Kolmogorov length scale η [54, 55], defined in Eq. 13.

$$\eta = \left(\frac{\nu^3}{\mathcal{E}}\right)^{1/4} \tag{13}$$

The dissipation rate, $\mathcal{E}$, is obtained from RANS k–$\mathcal{E}$–ζ–f [56] preliminary simulations and it is found to be in the order of $\mathcal{E} \simeq 10^9$ [m^2/s^3]. Considering the kinematic viscosity value ν being between 7.2 10^{-7} and 2.8 10^{-6} [m^2/s], respectively at 1 and 2,000 [bar], the resulting Kolmogorov length scale lays in the range of 1.4 10^{-7} and 4 10^{-7} [m]. The characteristic mesh size in the nozzle is then taken as 3 10^{-6} [m]. The characteristic cell size is evaluated as third root of average cell volume in the nozzle and the maximum aspect ratio is below 2. In order to correctly model the boundary layers, the mesh must undergo a special treatment in the near wall region. The first cell layer close to the wall should be within $y^+ = y/\ell_\tau < 1$ and at least 6 layers exist within $y^+ < 10$. An approximation for $\ell_\tau = \nu/u_\tau$ is also taken from preliminary RANS simulations: $\ell_\tau \simeq 3.2\ 10^{-8}$ [m]. The first cell layer close to the wall boundaries is then imposed to have a height of 3 10^{-8} [m], and the first 6 layers are within a distance of 3 10^{-7} [m] from the wall. This wall treatment is applied on the nozzle walls only.

The flow results showed that the ratio of SGS turbulence over total turbulence is below 15% in the most turbulent region inside the nozzle.

The final number of cells is in the order of 2 million. Second order time integration is applied with a time step of 3 [ns], corresponding to a convective Courant–Friedrichs–Lewy (CFL) number based on the flow characteristic velocity of 0.7. The whole modeled geometry and a detail of the mesh close to nozzle is presented in Fig. 1. With reference to the Fig. 1, the simulation boundary conditions are defined as shown in Tab. 1. The initial conditions are instead defined as described in Tab. 2 with zero velocity everywhere.

The needle lift profile measured in previous experiments and presented in [57] is shown in Fig. 2. The

Location	boundary condition type
Inlet (blue)	$p = 2,000$ [bar], $\alpha_l = 1$
Sides (red)	symmetry
Walls (grey)	no–slip velocity
Outlet (green)	$p = 60$ [bar]

Table 1: Boundary conditions summary with reference to Fig. 1.

Location	initial condition
Upstream the needle seat	$p = 2,000$ [bar], $\alpha_l = 1$
Needle seat, sac and nozzle	$p = 60$ [bar], $\alpha_l = 1$
Discharge volume	$p = 60$ [bar], $\alpha_g = 1$

Table 2: Initial conditions summary.

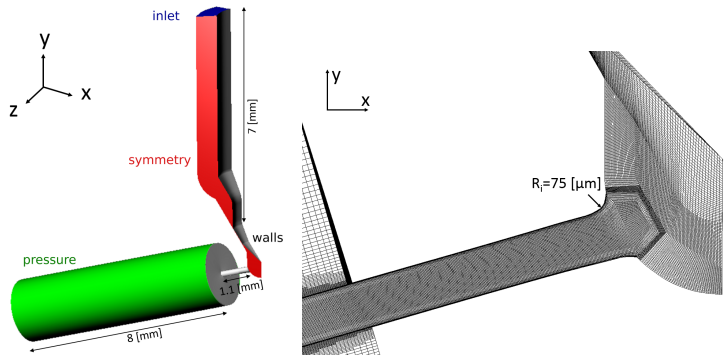

Figure 1: Injector mesh views: whole geometry with boundary conditions (left) and detail of the nozzle (right).

movement is modeled by stretching the cells between the needle and the needle seat; 32 cell layers are used in this region, with a minimum gap at the initial closed position of 2.5 [μm]. This allows to keep the same mesh for the entire simulation time. Due to the lack of measurements, a constant rail pressure is adopted.

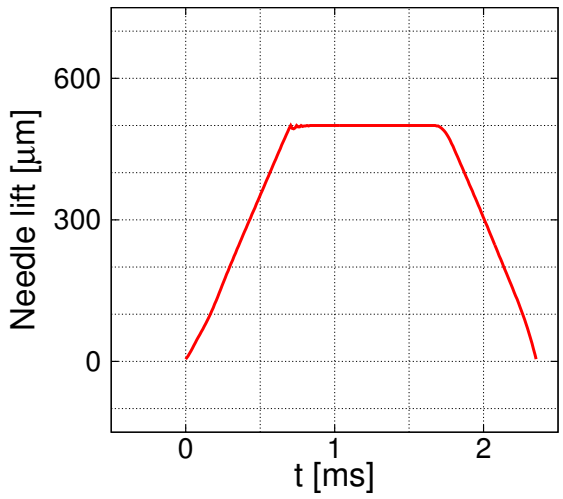

Figure 2: Needle lift profiles, reproduced from [57].

Evidences of material removal due to cavitation erosion were found in the experimental campaign.

X–rays visualization of the deformed internal geometry was presented in [57] and it is here reported in Fig 3. The deformation main characteristics, as extension and locations, are extracted from the available

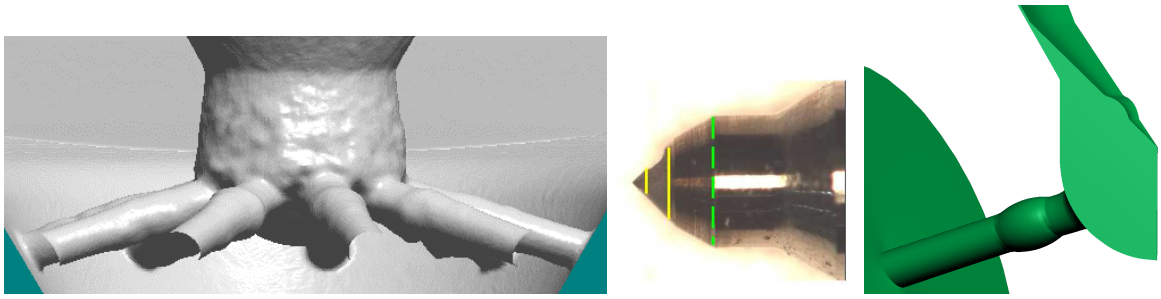

Figure 3: Cavitation erosion effect on the geometry, experimental visualization extracted from [57] (left and center) and deformed geometrical model (right).

pictures. The needle surface is deformed for a maximum depth of 25 [μm] at a location 140 [μm] above the needle tip. The nozzle is also deformed for a maximum depth of 25 [μm] at 300 [μm] downstream of the nozzle inlet. The resulting geometry is shown in Fig. 3. Results from two sets of simulations will then be compared: one obtained from the original injector with the nominal designed geometry and the second with the same conditions but a geometry deformed accordingly to the cavitation erosion patterns.

Fluid Properties. The flow is assumed to be isothermal with a fixed temperature of 150 [°C], neglecting viscous heating effects, which simplifies the problem complexity. The liquid fuel compressibility is modeled with the Tait equation of state; as known, this is an isentropic equation, based on a reference state and two experimentally determined parameters, B and n. The density is then computed with respect to the pressure as described in Eq. 14.

$$\rho(p) = \rho_{ref} \left\{ 1 + \frac{p - p_{ref}}{B} \right\}^{1/n} \tag{14}$$

The reference density, ρ_{ref}, was set to 723 [kg/m^3], the bulk modulus, B, to 100 [MPa] and the equation exponent n to 7.15 [–]. These parameters resulted in the best fit to experimental measurements of the used fluid. All obtained thermodynamic states correspond then to a temperature of 150 [°] with the liquid compressibility modeled with a barotropic relation having a speed of sound at the reference condition of $c_{ref} = \sqrt{\partial p/\partial \rho} = \sqrt{nB/\rho_{ref}} = 994$ [m/s]. The effect of the pressure on the liquid viscosity is also taken into consideration. In order to fit to experimental measurements, the viscosity, μ [mPas], is expressed as a third order polynomial with respect to the pressure,p [GPa], as: $\mu(p) = 0.5 + 7p - 2.5p^2 + 75p^3$. The variable fluid properties strongly affect the non–dimensional numbers that characterize the flow field, such as the Reynolds ($Re = UD\rho/\mu$) and Mach numbers ($M = U/c$). The Bernoulli velocity ($U = \sqrt{2\Delta p/\rho}$) can be computed as 677 and 729 [m/s] considering the fluid properties at 2,000 and 60 [bar], respectively. Correspondingly, the Reynolds number varies between 50,000 and 200,000 and the Mach number in the liquid phase only between 0.4 and 0.8. Air compressibility may play a role

in the spray formation; however, it can be neglected in the internal nozzle flow simulation due to the small influence of the chamber conditions on the internal flow. The air properties are then taken as constant at the chamber conditions of 60 [bar] and 150 [°C]: density of 49.8 [kg/m^3] and viscosity of 0.025 [mPas]. The fuel vapor is assumed to be incompressible at the saturation condition corresponding to $20,500$ [Pa] at 150 [°C]. A value for the viscosity of 0.5 [mPas] have been taken and the density value of 0.14 [kg/m^3] was computed from the ideal gas law. Considering the dominant effect of mass transfer on the liquid–vapor mixture compressibility [58, 26], vapor compressibility was neglected in order to reduce the problem complexity without losing the model prediction capabilities of cavitation phenomena.

Results and discussion

Mesh resolution

The effect of mesh resolution inside the nozzle is analyzed comparing the results of three simulations with completely open needle. Average flow results from three different meshes with increasing resolution are compared in Table 3. The *medium* grid main dimensions was discussed in the previous section, while the other two grids are generated either by increasing (*coarse*) or decreasing (*fine*) the characteristic cell size in the nozzle by a factor 2. All simulations had the same CFL number for the characteristic mesh size in the nozzle. The discharge coefficient, C_D, is obtained as shown in Eq. 15. The table shows that finer mesh resolution leads to smaller discharge coefficients and higher vapor presence. These results can be explained from the fact that more vapor is generated with the finer mesh due to a higher resolution of the flow field, including more cavitating turbulent structures. A different amount of vapor passing through the nozzle leads then to a significant change in the total mass flow due to the very low density of vapor compared to the one of the liquid. Even though no mesh convergence behavior is evident in the presented data, the relative difference in the discharge coefficient between the *medium* and the *fine* meshes is of 1%. In order to keep the computational cost of the entire injection simulation within feasible limits, the *medium* mesh has then been used for the results presented in the following sections.

$$C_D = \frac{\dot{m}}{\dot{m}_I} = \frac{\dot{m}}{A\sqrt{2\rho(p_{IN} - p_{OUT})}} \simeq \frac{\dot{m}}{17.7\ [\mathrm{g/s}]} \tag{15}$$

Mesh	*coarse*	*medium*	*fine*
Cell size in nozzle [μm]	6	3	1.5
Discharge coefficient [–]	0.824	0.817	0.809
Average mass flow [g/s]	14.6	14.47	14.33
Liquid volumetric flow ratio through the nozzle outlet [%]	97.03	96.83	95.75
Volumetric vapor content in nozzle [%]	5.53	5.55	6.25

Table 3: Mesh resolution effect, averaging time of 6 [μs] corresponding to 4 flow–through in the nozzle.

Macroscopic results

The results showing the discharge coefficient during the injection period are presented in Fig. 4. The graph shows that the acceleration period for the rate of injection ends at around 0.3 [ms] and the deceleration starts at 2.3 [ms] after start of injection. During this time interval, the discharge coefficient presents small oscillations around a constant value. With reference to Fig. 2 the two times coincide to a needle lift of 200 [μm], meaning that the flow is significantly obstructed in the needle seat region only for needle lifts below this value, while higher needle lifts do not lead to an increase in the mass flow. The percentage of nozzle volume occupied by vapor as function of time is also shown in Fig. 4. From this graph, it is evident that the applied geometry deformation due to the cavitation erosion, leads to a sensible decrease of the vapor volume in the nozzle. The reason for this effect can be explained from the

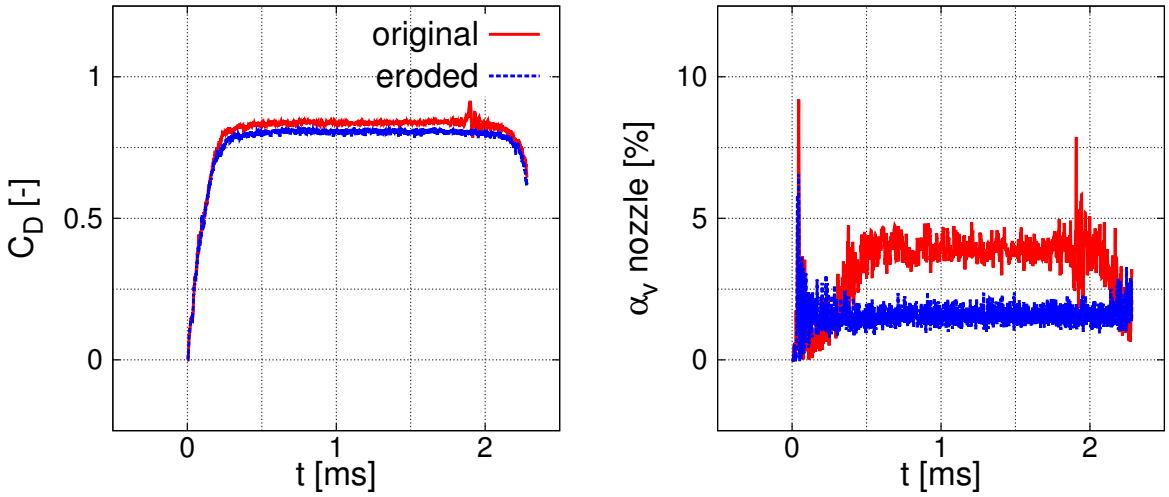

Figure 4: Discharge coeffcient and vapor volume percentage in nozzle during injection.

differences observed between the flow patterns in the two nozzles.

Time averaged macroscopic results for the fully open needle conditions are then presented in Table 4. A decrease in the discharge coefficient of the order of 3.8% is caused by the geometry deformation on

	original	*eroded*
Discharge coefficient [–]	0.837 ± 0.010	0.806 ± 0.007
Volumetric vapor content in nozzle [%]	3.82 ± 0.53	1.55 ± 0.24
Volumetric vapor flow ratio [%]	1.02 ± 0.73	0.90 ± 0.73

Table 4: Statistical results comparison, average values with relative standard deviation during the fully open needle interval.

the needle and the nozzle. This is caused by the local contraction of the flow passage area due to the wider flow recirculation in correspondence to the erosion locations in the nozzle; further details are given in the following analyses on the internal nozzle flow. The amount of vapor generated inside the nozzle decreases significantly, so that the eroded injector shows less than half of the vapor in the nozzle compared to the non–deformed geometry. However, the difference is reduced significantly at the nozzle outlet, where in both cases only 1% of volumetric flow is occupied by vapor. These data indicate that the erosion deformation damps significantly the vapor cavity formed close to the nozzle inlet, however does not influence the vapor cavities formed inside the nozzle and convected outside.

Flow field results

Indicative samples of the nozzle flow at fully open needle are presented in Fig. 5 for both the eroded and non–eroded geometries. These specific time steps are selected as the ones at which the main flow field features are the most clearly visible and do not deviate significantly from the average flow. The vapor cavity fills the recirculation zone that starts at the upper part of nozzle inlet and extends up to $50\% - 80\%$ of the nozzle length. This region extends for circa 90° around the nozzle hole circumference. Two counter–rotating vortices are formed below the recirculation region; these start to cavitate at $30\% - 50\%$

of the nozzle length. Their exact location and extension is strongly perturbed by the unsteady upstream flow, resulting in a transient behavior. These flow patterns are significantly different in the eroded geometry. The nozzle hole expansion section due to erosion leads to a local decrease in the velocity and thus recovering of the pressure. This leads to a much shorter vapor cavity on the upper side of the nozzle inlet. However, a second vapor cavity appears on the lower side of the nozzle just after the eroded part. The local increase and decrease in the nozzle section area generates a vorticity component along the nozzle circumference that causes a recirculation region starting from the lower lip of the deformed section on the downstream side ($\overline{w}_\theta = \partial \overline{v}_r / \partial h$, with θ being the angular coordinate of the nozzle circumference, r the distance from the nozzle axis and h the coordinate traveling along the nozzle axis). An attached sheet vapor cavity fills this recirculation zone and extends for $20\% - 40\%$ of the nozzle length. This region extends for circa $270°$ around the nozzle hole circumference. Vapor cavities detach from this region and are convected downstream. In this flow patterns cavitating vortices still appear, but their presence is negligible compared to the ones formed in the non–eroded geometry. The absence of the long vapor cavity on the upper side of the nozzle inlet for fully open needle conditions leads then to an overall smaller vapor quantity in the eroded geometry compared to the original one; these differences explain the results presented in Fig. 4. A major effect of the eroded nozzle is visible in the velocity cut close to the nozzle outlet: the eroded geometry shows a less uniform velocity field. This is expected to affect the formed spray.

Cavitation erosion predictions

The risk of cavitation erosion is predicted by recording the pressure peaks generated by the collapse of vapor cavities. The time evolution of recorded pressure peaks on the surfaces shows that the strongest collapse events (above the inlet pressure of $2,000$ [bar]) happen at low needle lifts. Since the flow field varies significantly during the needle opening and closing phases, pressure peaks appearance locations change during the injection. Figure 6 shows the pressure peaks recorded on the bottom of the nozzle and on the needle at 0.15 [ms] after start of injection on the original geometry. During the beginning of the injection event, vapor cavities are formed along the needle due to the initial movement. The collapse of these vapor cavities leads to pressure peaks on the needle surface in locations similar to the one detected by the experiments (see Fig. 3). The pressure peaks on the bottom of the nozzle are instead generated by the vapor cavities detached from the lower lip of the nozzle inlet during the initial flow acceleration period. In fact, when the flow is still developing inside the sac region, the highest flow acceleration appears on the lower side of the nozzle inlet. On the top side on the nozzle, most of the recorded pressure peaks appear instead between 0.15 [ms] and 0.3 [ms] from the start of injection. The distribution of recorded pressure peaks does not change significantly for the rest of the needle opening phase and injection phase. A few new pressure peaks appear then also during the needle closing phase between 2.2 [ms] and 2.3 [ms]. Both time intervals correspond to needle lift values between

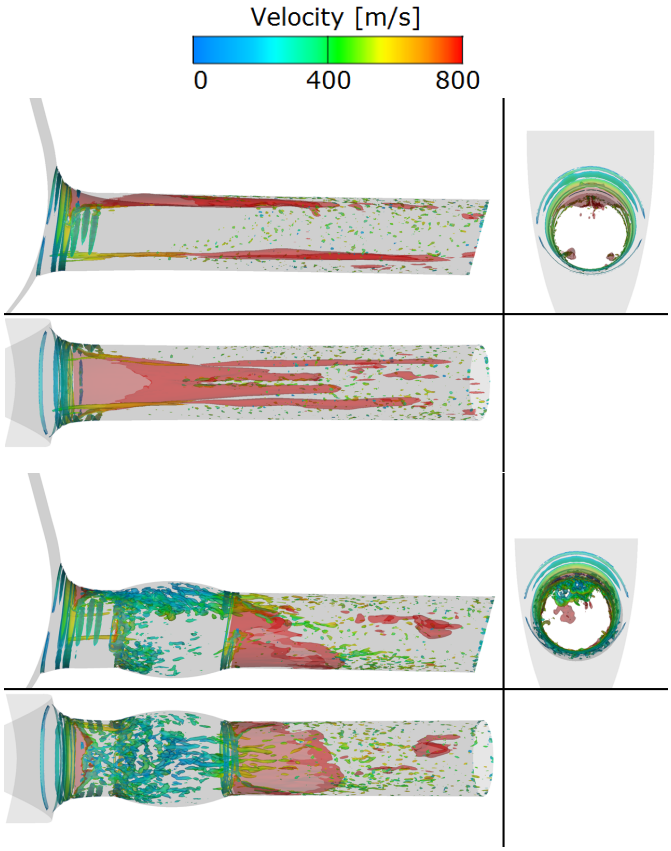

Figure 5: Indicative instantaneous flow field distribution at fully open needle valve conditions: original (above) and eroded (below) geometries. Orthogonal projection of 50% vapor iso–surfaces (red) and Q–invariant iso–surfaces at 1.5 10^{14} [s^{-2}] colored with velocity values.

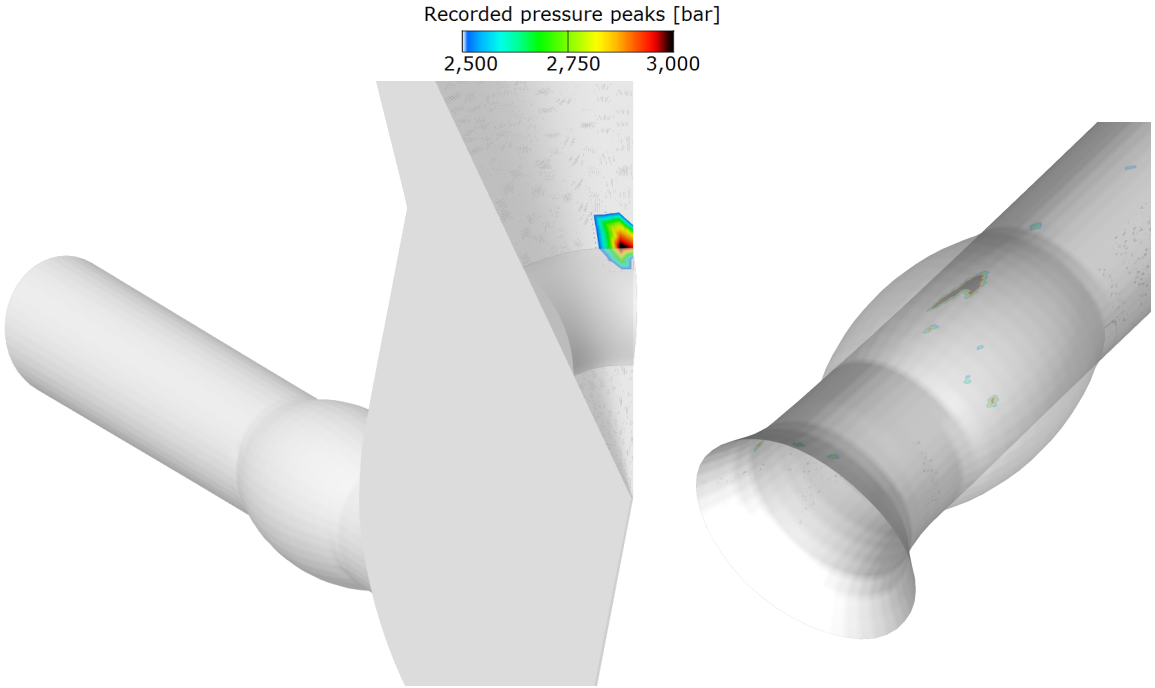

Figure 6: Recorded pressure peaks at 0.15 [ms] after start of injection: needle (left) and nozzle bottom (right). The simplified geometry of the eroded injector is overlapped with a transparent surface for visual impression of the damage locations.

100 and 200 [μm] and they coincide with the instants of the highest change in the slope of the rate of injection. From these observations, it is possible to conclude that the highest cavitation erosion risk for the presented injector happens when the needle movement stops or starts influencing the nozzle flow, and then when the highest curvature in the rate of injection is visible. At these conditions, the velocity magnitude is the same as the one at the fully open needle conditions but the flow field is still under development due to the effect of the moving needle (opening or closing). In Fig. 7 the pressure peaks distribution on the top side of the nozzle at the times 0.15, 0.3, 2.2 and 2.3 [ms] after start of injection are presented together with the results at the end of the injection overlapped by a transparent surface of the simplified model of the eroded geometry. Cavitation erosion patterns change during the material

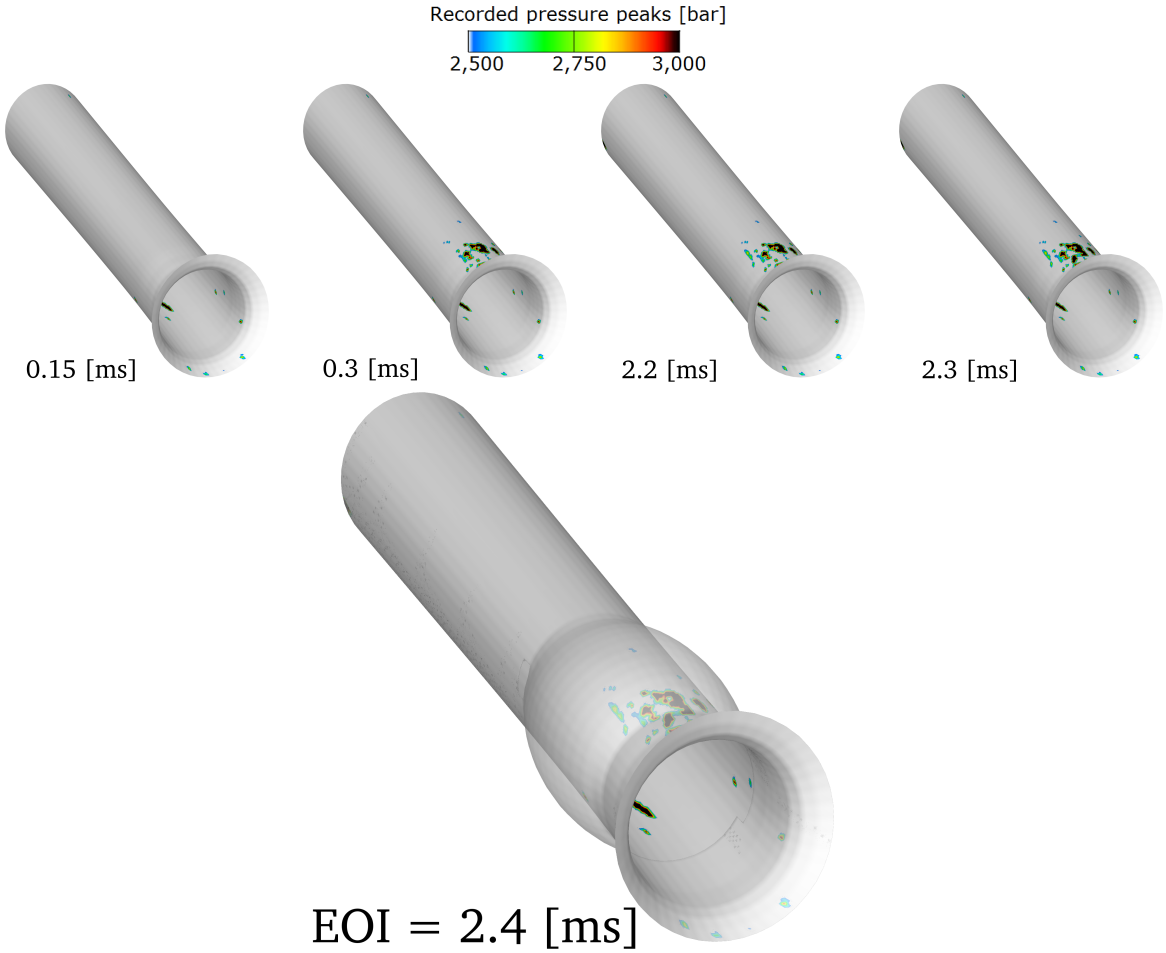

Figure 7: Recorded pressure peaks at the end of the injection on the top of the nozzle. From left to right above results at 0.15, 0.3, 2.2 and 2.3 [ms] after start of injection and below results at the end of injection (EOI) overlapped by the model of the eroded nozzle.

removal process due to the influence of geometry deformation on the flow [7]. The presented results can then be related only with the initial phase of the erosion process. The beginning of material removal leading to the geometry shown in Fig. 3 can be expected to be in good agreement with the locations of recorded pressure peaks on the top side of the nozzle. Erosion on the side of the nozzle is instead expected to be caused mainly by asymmetric flow characteristics, such as hole–to–hole flow variations

and eccentric needle motion. The lack of experimental data in terms of needle movement normal to the needle axis, as well as real geometry deviations from the nominal design of each nozzle hole, does not allow to predict erosion in these locations with the current simulation.

Time averaged nozzle flow fields

The flow is intrinsically unsteady due to the moving needle, however the time averaged flow fields at the nozzle exit may provide useful indications about the internal nozzle flow and its influence on spray formation. Fig. 8 shows the average flow fields at the nozzle outlet, corresponding to the plane where the internal nozzle flow is provided as boundary condition for the subsequent spray simulations. The velocity magnitude, velocity rms and projected velocity vectors are presented together with the average vapor volume fraction presence for both, the original and eroded geometries. The main visible differences appear in the upper part of nozzle outlet where the eroded injector shows a bigger area with lower velocity and velocity fluctuations, as well as a more spread vapor presence. Furthermore, the two counter rotating vortices visible from the projected velocity vectors, show different locations between the original and eroded injectors.

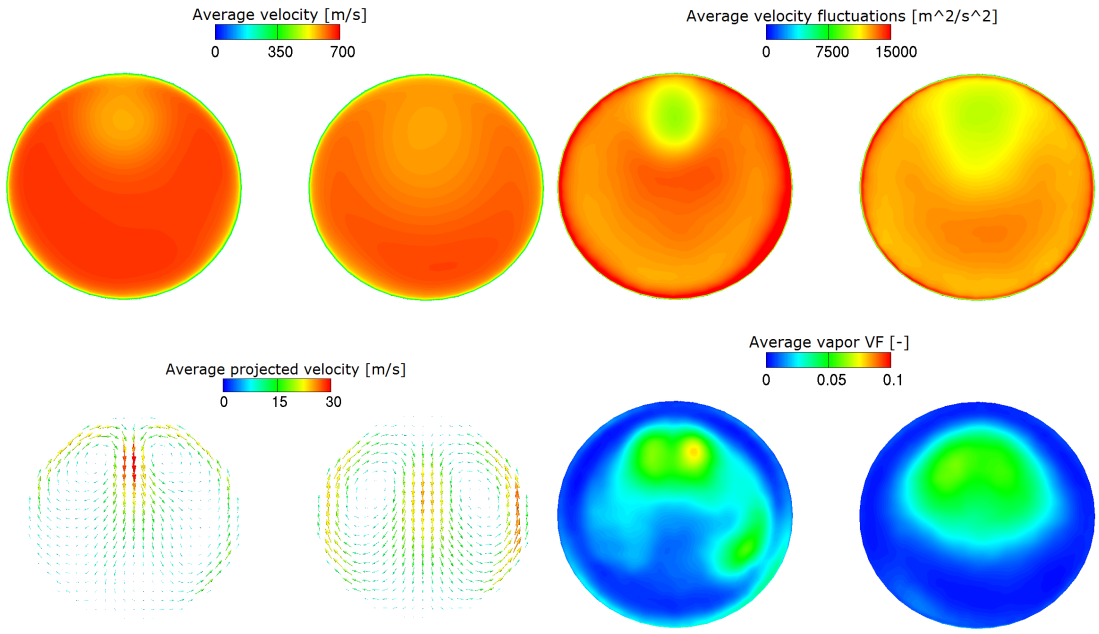

Figure 8: Time averaged over the whole injection period flow field at the nozzle outlet: velocity magnitude, velocity rms, projected velocity vectors and vapor volume fraction. Comparison between original nozzle (left) and eroded nozzle (right).

Figure 9 shows the flow distribution on the nozzle hole symmetry plane. The average vapor volume fraction iso–line of 6% is shown with the black continuous line while six velocity profiles are included with a red dash–dotted line; moreover the boundary layer thickness (δ_{99}) on the lower side on the nozzle is presented with the dashed white line computed as the location for which $\bar{u}(\delta_{99}) = 0.99U_l$. In both cases the flow recirculation leads to the formation of a slower area on the upper side, that starts after the inlet and whose centre moves towards the nozzle axis. In the original geometry, this portion is partially filled with vapor. In the eroded geometry, the local section expansion decelerates the flow and causes boundary layer detachment from the wall on the upper side. The successively convergent shape moves the slow velocity region further away from the wall compared to the original geometry. In the eroded

geometry, a cavitation inception zone exist in the low velocity region detached from the wall. Another difference can also be detected by looking to the boundary layer thickness profile on the lower side of the nozzle: the erosion deformation leads to a local increase in the boundary layer thickness and, after it is reattached to the wall, it is partially filled with vapor. However, in both cases, it can be seen that the boundary layer thickness never reaches the channel axis. The nozzle length is then too short to obtain a fully developed turbulent flow and, at the nozzle outlet, the flow is still in a developing stage. This is in good agreement with the theory for the entry length of turbulent pipe flows that predicts a length 5 times longer than the actual nozzle length $l_h \simeq 1.359 D Re^{1/4} \simeq 5$ [mm] [59].

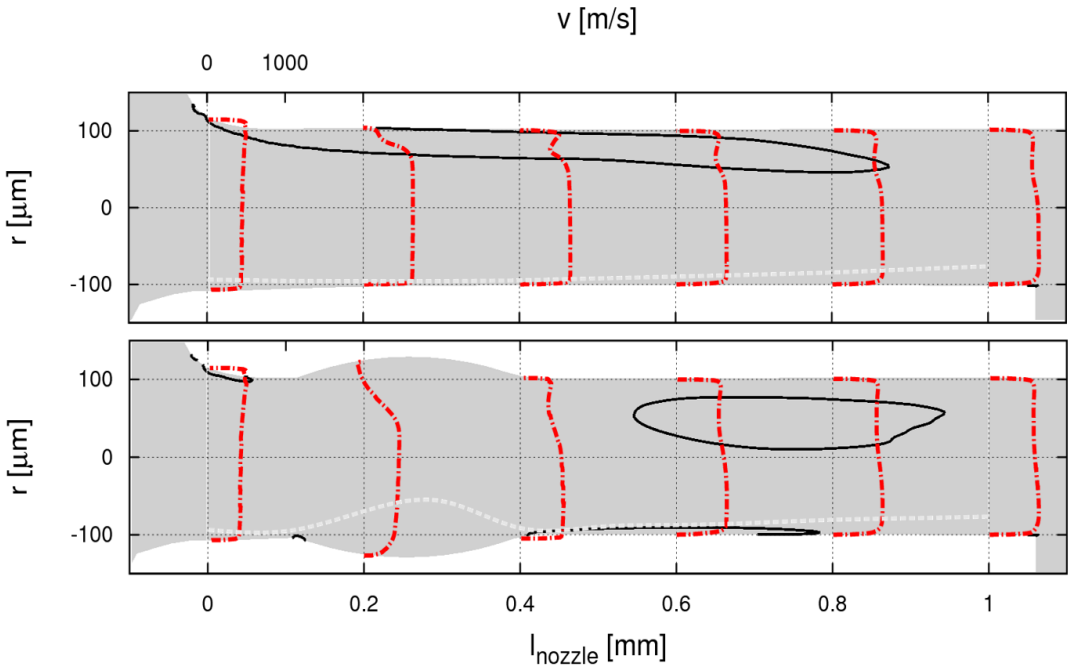

Figure 9: Time averaged vapor volume fraction (black iso–line representing 6%), velocity profiles along the nozzle (dash–dots red line) and boundary layer thickness on the lower side (dashed white line) of the original (top) and eroded (bottom) geometry.

In Fig. 10 the average velocity profiles at three locations are presented, for both the eroded and not eroded injectors. This allows to compare the average velocity magnitude along the nozzle length. Two main differences between the original and the eroded geometry can be detected. The inlet profile of the eroded geometry is already influenced by the downstream presence of the expansion: the flow decelerates and the recirculation region is further deviated from the wall. In the *mid–distance* and *outlet* profiles, the low velocity region is spread sooner in the eroded geometry. The integral value of the velocity at the outlet is smaller for the eroded injector, thus explaining the loss in discharge coefficient seen in Fig. 4.

Spray simulations results

The aim of this section is to analyze the effect of changes in the geometry due to cavitation erosion on the spray primary break–up and near–nozzle spray dispersion. Non–reacting spray simulations have been performed which are using the flow at the nozzle outlet computed from the internal injector flow

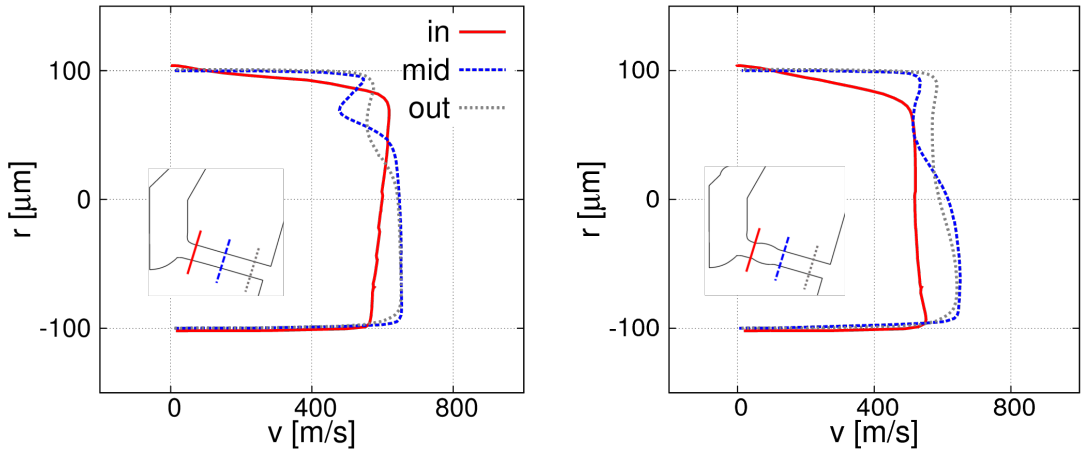

Figure 10: Time averaged velocity profiles at three locations along the nozzle for the original geometry (left) and the eroded (right). The three locations are respectively 100 [μm] downstream the nozzle inlet (*in* with red continuous line), 500 [μm] (*mid* with blue dashed line) and at 900 [μm] (*out* with grey dotted line).

simulations as inlet conditions [60, 61, 62, 63, 64]. Two spray simulations have been performed, one starting from the internal nozzle flow of the original injector geometry and one from the one affected by erosion; unfortunately, as there are no experimental data for the simulated injectors, the results presented here aim to offer a comparative study on the possible effects of nozzle hole erosion on spray development. The sprays are realized in an unbounded volume at typical in–cylinder conditions for Diesel engines corresponding to 900 [K] and 60 [bar] (air density of 23.1 [kg/m^3]) [65, 66]. The injected fluid is considered incompressible, while air compressibility has been taken into account. The computational mesh consists of 500, 000 hexaedral cells, and the used time step is of 650 [ns], corresponding to a characteristic convective CFL number of 3.5.

Due to the lack of experimental data for the presented simulations and the arbitrariness of some model tuning coefficients, a parameter influence analysis on the main tuning coefficient has been done. The constant C_2 scales the characteristic break–up time of the WAVE model [53] and may vary from one injector to another to accommodate the model uncertainties. As visible from the Table 5, longer break–up times leads to longer spray tip penetration lengths. Results show that even though major differences are visible, the same trend exists comparing the original and the eroded nozzle. In the following analyses the mid-value, $C_2 = 9$, has been considered.

	original	*eroded*
$C_2 = 6$	8.1	7.8
$C_2 = 9$	10.1	9.4
$C_2 = 20$	18.7	17.1

Table 5: Effect of the WAVE model coefficient C_2 on the liquid penetration length of the spray center of mass in [mm]. Time averaged values between 1 and 1.8 [ms].

The spray tip penetration and the spray angle are plotted in Fig. 11. Two estimates for the spray penetration are shown: one is computed considering the average distance from the nozzle outlet of the

furthest 1% of liquid mass in the spray, and the second one is the distance of the entire spray centre of mass. The trends presented in Fig. 11 shows no visible difference between the two cases during the starting phase of the injection; however the liquid penetration at fully open needle conditions shows that the eroded injector creates a shorter spray than the injector with the nominal geometry. The difference in the average penetration lengths is for both values in the order of 0.7 [mm], corresponding to 3.5% for the furthest 1% of spray and 7% for the spray centre of gravity.

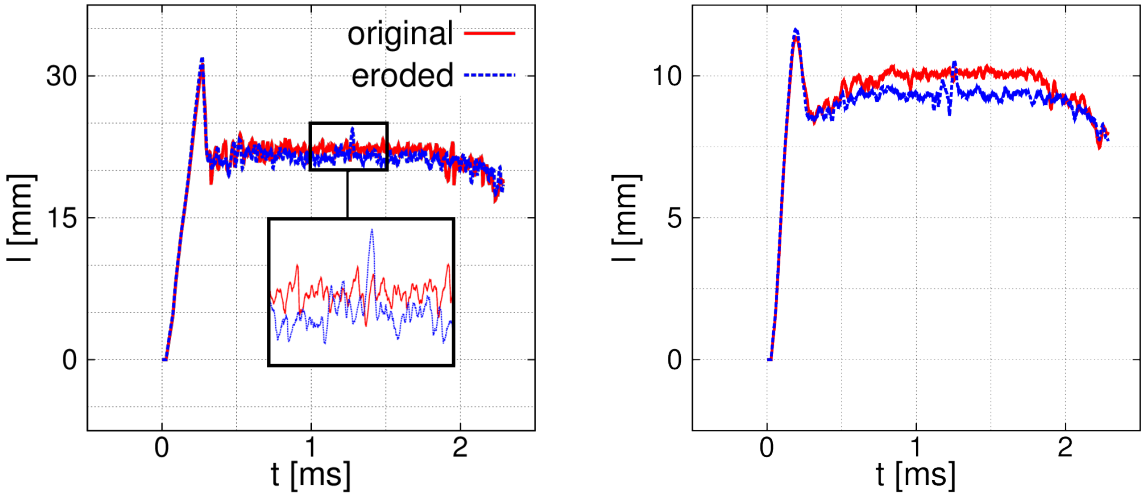

Figure 11: Liquid penetration length comparison between original (continuous red line) and eroded (dashed blue line) geometries. Penetration length presented as the furthest 1% (left) and the spray center of mass (right).

The average spray angle value has been obtained applying a weighting coefficient proportional to the droplet's mass to the angle of each droplet respect to spray axis. The results are plotted in Fig. 12. Similar to the spray penetration length, no clear difference trend is visible during the spray initial stages but a wider spray angle is visible in the eroded nozzle at fully open needle. In this case the relative difference is around 15%.

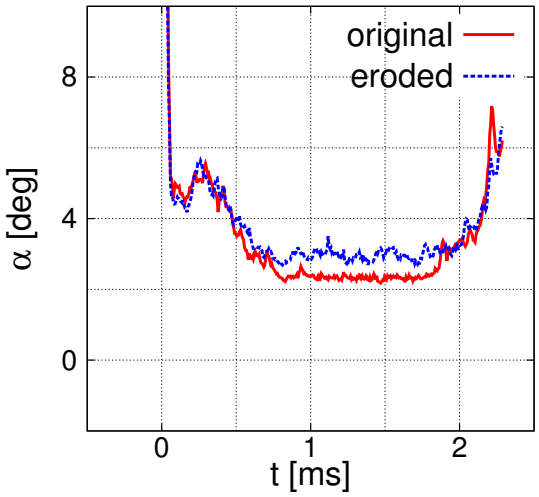

Figure 12: Spray angle comparison between original (continuous red line) and eroded (dashed blue line) geometries.

For both cases a quasi–steady spray pattern could be identified between 1 and 1.8 [ms]. Average values of penetration length and spray angle could then be extracted in this time interval in order to provide a comparison between the two cases in Table 6.

	original	*eroded*
Liquid penetration length of the furthest 1% liquid mass [mm]	22.2 ± 0.3	21.4 ± 0.6
Liquid penetration length of the spray center of mass [mm]	10.1 ± 0.1	9.4 ± 0.3
Spray angle [°]	2.33 ± 0.06	2.97 ± 0.14

Table 6: Penetration lengths and spray angle average values between 1 and 1.8 [ms] with relative standard deviation.

Conclusions

In the presented work, a compressible pressure–based multi–phase solver is used to study the effect of geometry deformation caused by cavitation erosion in a Diesel injector. The numerical algorithm is initially presented, with emphasis to the cavitation, momentum coupling and liquid compressibility models. The comparison of simulation results between the injectors with the nominal designed geometry and with eroded geometry (as detected by previous experiments) shows that cavitation erosion leads to significant differences in the flow. A main injection event is simulated modeling the longitudinal needle movement as measured by the experiments. The flow field main characteristics are then analyzed, both at the start of injection and for fully open needle conditions. The eroded injector shows a 3.8% average loss of performances for the rate of injection. Locations of pressure peaks recorded on the walls due to collapsing vapor cavities show a good agreement with the actual erosion patterns visible from the experiments. The most intense events are mainly recorded in the opening phase for needle lift values below 200 [μm], when the stable sheet cavity is still not formed and the flow is highly fluctuating in the recirculation zone close to the nozzle inlet. Internal nozzle flow results are then used to define the inlet conditions of non–reactive spray simulations with the Lagrangian approach in a RANS simulation. The differences in the nozzle outlet flow are then reflected in a shorter and wider spray for the eroded injector. The significant influence of geometry deformation due to erosion indicates the importance of correctly modeling the exact internal geometry, so that x–rays scan of the actual injector used during the experiments is also crucial to correctly model the internal injector flow. The importance of modeling the needle motion is also evident by the transient nature of the results and the inclusion of 3–D needle movement would further improve the cavitation erosion risk assessment capabilities.

Acknowledgements

Financial support from the MSCA–ITN–ETN of the European Union H2020 programme, under REA grant agreement n. 642536 is acknowledged. The authors acknowledge the support of my colleagues Jure Strucl and Mandumpala Devassy Bejoy for the technical support for the creation of the meshes.

References

[1] Van Basshuysen R., Schäfer F. Internal combustion engine handbook–basics, components, systems and perspectives; vol. 345. SAE; 2004. ISBN 0768011396.

[2] Bosch Electronic Automotive Handbook. 7ed.; John Wiley & Sons; 2007. ISBN 9780470519363.

[3] Egler W., Giersch R.J., Boecking F., Hammer J., Hlousek J., Mattes P., et al. Fuel injection systems. In: Mollenhauer K., Tschoeke H., editors. Handbook of Diesel Engines. Springer–Verlag Berlin Heidelberg. ISBN 9783540890829; 2010,.

[4] Dular M., Stoffel B., B. S. Development of a cavitation erosion model. Wear2006;261:642–55. Http://dx.doi.org/10.1016/j.wear.2006.01.020.

[5] Bark G., Grekula M., Bensow R.E., Berchiche N. On some physics to consider in numerical simulation of erosive cavitation. In: 7th International Symposium on Cavitation. Ann Arbor, Michigan, USA; 2009,.

[6] Sezal I.H., Schmidt S.J., Schnerr G.H., Thalhamer M., Förster M. Shock and wave dynamics in cavitating compressible liquid flows in injection nozzles. Shock Waves2009;19(1):49–58. Https://doi.org/10.1007/s00193-008-0185-3.

[7] Skoda R., Iben U., Mozorov A., Mihatsch M., Schmidt S.J., Adams N.A. Numerical simulation of collapse induced shock dynamics for the prediction of the geometry, pressure and temperature impact on the cavitation erosion in micro channels. In: WIMRC, 3rd International Cavitation Forum. University of Warwick; 2011,.

[8] Skoda R., Iben U., Güntner M., Schilling R. Comparison of compressible explicit density–based and implicit pressure–based cfd methods for the simulation of cavitating flows. In: 8th International Symposium on Cavitation. Singapore; 2012,Http://dx.doi.org/10.1016/j.compfluid.2011.11.003.

[9] Fortes-Patella R., Archer A., Flageul C. Numerical and experimental investigations on cavitation erosion. In: Earth I.C.S., 15 E.S., editors. 26th IAHR Symposium on Hydraulic Machinery and Systems. 2012,Http://doi:10.1088/1755-1315/15/2/022013.

[10] Pöhl F., Mottyll S., Skoda R., Huth S. Evaluation of cavitation–induced pressure loads applied to material surfaces by finite–element–assisted pit analysis and numerical investigation of the elasto–plastic deformation of metallic materials. Wear2015;330–331:618–28. Http://dx.doi.org/10.1016/j.wear.2014.12.048.

[11] Mihatsch M.S., Schmidt S.J., Adams N.A. Cavitation erosion prediction based on analysis of flow dynamics and impact load spectra. Physics of Fluids2015;27(103302). Http://dx.doi.org/10.1063/1.4932175.

[12] Koukouvinis P., Bergeles G., Gavaises M. A cavitation aggressiveness index within the Reynolds averaged Navier Stokes methodology for cavitating flows. Journal of Hydrodynamics2015;27(4):579–86. Http://dx.doi.org/10.1016/S1001-6058(15)60519-4.

[13] Koukouvinis P., Karathanassis I.K., Gavaises M. Prediction of cavitation and induced erosion inside a high–pressure fuel pump. In: of Engine Research I.J., editor. IMechE. 2017, p. 1–14. Http://dx.doi.org/10.1177/1468087417708137.

[14] Ghahramani E., Arabnejad M.H., Bensow R.E. Realizability improvements to a hybrid mixture–bubble model for simulation of cavitating flows. Computers & Fluids2018;174:135–43. Https://doi.org/10.1016/j.compfluid.2018.06.025.

[15] Schenke S., Melissaris T., van Terwisga T.J.C. On the relevance of kinematics for cavitation implosion loads. Physics of Fluids2019;31(052102). Https://doi.org/10.1063/1.5092711.

[16] Grogger H.A., Alajbegović A. Calculation of the cavitating flow in Venturi geometries using two fluid model. In: FEDSM A., editor. ASME Fluids Engineering Division Summer Meeting. Washington, D. C., USA; 1998,.

[17] Arcoumanis C., Gavaises M. Cavitation in diesel injectors: modelling and experiments. In: ILASS–EUROPE. Manchester, UK; 1998,.

[18] Alajbegović A., Grogger H.A., Philipp H. Calculation of transient cavitation in nozzle using the two–fluid model. In: 12th Annual Conference on Liquid Atomization , Systems S., editors. ASME Fluids Engineering Division Summer Meeting. Indianapolis, Indiana, USA; 1999,.

[19] Roth H., Giannadakis E., Gavaises M., Arcoumanis C., Omae K., Sakata I., et al. Effect of multi–injection strategy on cavitation development in diesel injector nozzle holes. SAE Transactions Journal Of Engines2005;114(3):1029–45.

[20] Andriotis A. Gavaises M. Influence of vortex flow and cavitation on near–nozzle diesel spray dispersion angle. Atomization and Sprays2009;19(3):247–61. Http://dx.doi.org/10.1615/AtomizSpr.v19.i3.30.

[21] Reid B.A., Hargrave G.K., Garner C.P., Wigley G. An investigation of string cavitation in a true–scale fuel injector flow geometry at high pressure. Physics of Fluids2010;22(031703). Https://doi.org/10.1063/1.3372174.

[22] Mitroglou N., Gavaises M. Cavitation inside real–size fully transparent fuel injector nozzles and its effect on near–nozzle spray formation. In: DIPSI workshop on droplet impact phenomena and spray investigations. University of Bergamo, Italy; 2011,.

[23] Gavaises M., Villa F., Koukouvinis P., Marengo M., Franc J.P. Visualisation and LES simulation of cavitation cloud formation and collapse in an axisymmetric geometry. International Journal of Multiphase Flow2015;68:14–26. Http://dx.doi.org/10.1016/j.ijmultiphaseflow.2014.09.008.

[24] Egerer C.P., Hickel S., Schmidt S.J., Adams N.A. Large–eddy simulation of turbulent cavitating flow in a micro channel. Physics of Fluids2014;26(085102):190–200. Http://dx.doi.org/10.1063/1.4891325.

[25] Koukouvinis P., Gavaises M., Li J.Z., Wang L. Large eddy simulation of diesel injector including cavitation effects and correlation to erosion damage. Fuel2016;175:26–39. Http://dx.doi.org/10.1016/j.fuel.2016.02.037.

[26] Koukouvinis P., Mitroglou N., Gavaises M., Lorenzi M., Santini M. Quantitative predictions of cavitation presence and erosion–prone locations in a high–pressure cavitation test rig. Journal of Fluid Mechanics2017;819:21–57. Http://dx.doi.org/10.1017/jfm.2017.156.

[27] Cristofaro M., Edelbauer W., Gavaises M., Koukouvinis P. Numerical simulation of compressible cavitating two–phase flows with a pressure–based solver. In: ILASS–Europe, 28th Conference on Liquid Atomization and Spray Systems. Valencia, Spain; 2017,Http://dx.doi.org/10.4995/ILASS2017.2017.4629.

[28] Cristofaro M., Edelbauer W., Koukouvinis P., Gavaises M. Large eddy simulation of the internal injector flow during pilot injection. In: Proceedings of the 10th International Symposium on Cavitation. Baltimore, MD, USA: ASME Press; 2018,Https://dx.doi.org/10.1115/1.861851.

[29] Gavaises M., Andriotis A. Cavitation inside multi–hole injectors for large diesel engines and its effect on the near–nozzle spray structure. Transactions Journal of Engines, SAE Paper 2006–01–11142006;115–3:634–47. Https://doi.org/10.4271/2006-01-1114.

[30] Andriotis A., Gavaises M., Arcoumanis C. Vortex flow and cavitation in diesel injector nozzles. Journal of Fluid Mechanics2008;610:195–215. Https://doi.org/10.1017/S0022112008002668.

[31] Shi J., Gomez Santos E., Hoffmann G., Dober G. Large eddy simulation as an effective tool for gdi nozzle development. MTZ worldwide2018;79(10):58–63. Https://doi.org/10.1007/s38313-018-0089-2.

[32] Lešnik L., Kegl B., Bombek G., Hočevar M., Biluš I. The influence of in–nozzle cavitation on flow characteristics and spray break–up. Fuel2018;222:550–60. Https://doi.org/10.1016/j.fuel.2018.02.144.

[33] Edelbauer W., Strucl J., Morozov A. Large eddy simulation of cavitating throttle flow. In: SimHydro: Modelling of rapid transitory flows. Sophia Antipolis, F; 2014,.

[34] Lechner C., Lauterborn W., Koch M., Mettin R. Fast, thin jets from bubbles expanding and collapsing in extreme vicinity to a solid boundary: A numerical study. Physical Review Fluids2019;4(021601). Https://doi.org/10.1103/PhysRevFluids.4.021601.

[35] Schmidt S.J., Mihatsch M., Thalhamer M., Adams N.A. Assessment of the prediction capability of a thermodynamic cavitation model for the collapse characteristics of a vapor–bubble cloud. In: WIMRC, 3rd International Cavitation Forum. University of Warwick; 2011,.

[36] Schenke S., van Terwisga T.J.C. Simulating compressibility in cavitating flows with an incompressible mass transfer flow solver. In: Fifth International Symposium on Marine Propulsors. Espoo, Finland; 2017, p. 71–9.

[37] Patankar S.V., Spalding D.B. A calculation procedure for heat, mass and momentum transfer in three-dimensional parabolic flows. International Journal of Heat and Mass Transfer1972;15(10):1787–806.

[38] Lord Rayleigh J.W.S. On the pressure developed in a liquid during the collapse of a spherical cavity. Philosophical Magazine Series 61917;34(200):94–8. Http://dx.doi.org/10.1080/14786440808635681.

[39] Plesset M.S. The dynamics of cavitation bubbles. ANSME Journal of Applied Mechanics1949;16:228–31.

[40] Wood A.B. A textbook of sound: Being an account of the physics of vibrations with special reference to recent theoretical and technical developments. Macmillan; 1930.

[41] Kobayashi H. The subgrid–scale models based on coherent structures for rotating homogeneous turbulence and turbulent channel flow. Physics of Fluids2005;17(045104).

[42] Schiller L., Naumann A.Z. Über die grundlegenden berechnungen bei der schwerkraftaufbereitung. Z Vereines Deutscher Inge1933;77:318–21.

[43] Grinstein F.F., Margolin L.G., Rider W.J. Implicit large eddy simulation: computing turbulent fluid dynamics. Cambridge university press; 2007. ISBN 9780511618604. Https://doi.org/10.1017/CBO9780511618604.

[44] Schmidt S.J., Mihatsch M., Thalhamer M., Adams N.A. Assessment of Erosion Sensitive Areas via Compressible Simulation of Unsteady Cavitating Flows; vol. 106. Springer Science & Business Media. ISBN 9789401785396; 2014,.

[45] Gaskell P.H., Lau A.K.C. Curvature–compensated convective transport: Smart, a new boundedness–preserving transport algorithm. International Journal for numerical methods in fluids1988;8(6):617–41. Https://doi.org/10.1002/fld.1650080602.

[46] Sweby P.K. High resolution schemes using flux limiters for hyperbolic conservation laws. SIAM journal on numerical analysis1984;21(5):995–1011.

[47] Software User Manual. AVL FIRE™ ; 2018.

[48] von Berg E., Edelbauer W., Alajbegovic A., Tatschl R., Volmajer M., Ganippa L.C. Coupled simulations of nozzle flow, primary fuel jet breakup, and spray formation. Journal of Engineering for Gas Turbines and Power2004;127(4):0742–4795. Http://dx.doi.org/10.1115/1.1914803.

[49] Mandumpala Devassy B., Edelbauer W., Greif D. Study of cavitation and 3d needle movement due to erosion in fuel injection nozzles using coupled simulation tools. In: 18th Annual Conference on Liquid Atomization and Spray Systems. Chennai, India: ILASS–Asia; 2016,.

[50] Launder B.E., Spalding D.B. The numerical computation of turbulent flows. Computer Methods in Applied Mechanics and Engineering1974;3(2):269–89. Https://doi.org/10.1016/0045-7825(74)90029-2.

[51] Tatschl R., von Künsberg Sarre C., Alajbegović A., Winklhofer E. Diesel spray break–up modeling including multidimensional cavitating nozzle flow effects. In: ILASS–Europe. Darmstadt, DE; 2000,.

[52] Abramzon B., Sirignano W.A. Droplet vaporization model for spray combustion calculations. International journal of heat and mass transfer1989;32(9):1605–18.

[53] Liu A.B., Mather D., Reitz R.D. Modeling the effects of drop drag and breakup on fuel sprays. SAE Technical Paper1993;(930072):83–95. Https://doi.org/10.4271/930072.

[54] Fröhlich J., Mellen C.P., Rodi W., Temmerman L., Leschziner M.A. Highly resolved large–eddy simulation of separated flow in a channel with streamwise periodic constrictions. Journal of Fluid Mechanics2005;526:19–66. Https://doi.org/10.1017/S0022112004002812.

[55] Šarić S., Jakirlić S., Breuer M., Jaffrézic B., Deng G., Chikhaoui O., et al. Evaluation of detached eddy simulations for predicting the flow over periodic hills. In: ESAIM: proceedings; vol. 16. 2007, p. 133–45. Https://doi.org/10.1051/proc:2007016.

[56] Basara B. An eddy viscosity transport model based on elliptic relaxation approach. AIAA Journal2006;44:1686–90.

[57] Greif D., Srinivasan V. Numerical prediction of erosive cavitating flows in injection equipment. In: 10th International Conference on Engines and Vehicles. Capri, Italy; 2011,Http://dx.doi.org/10.4271/2011-24-0004.

[58] Franc J.P., Michel J.M. Fundamentals of cavitation; vol. 76. Springer Science & Business Media. ISBN 9781402022333; 2005,.

[59] Shah R.K., Bhatti M.S. Laminar convective heat transfer in ducts; vol. 3of *Handbook of single–phase convective heat transfer*. Wiley, New York; 1987.

[60] López J.J., Salvador F.J., de la Garza O.A., Arrègle J. A comprehensive study on the effect of cavitation on injection velocity in diesel nozzles. Energy Conversion and Management2012;64:415–23. Https://doi.org/10.1016/j.enconman.2012.03.032.

[61] He Z., Tao X., Zhong W., Leng X., Wang Q., Zhao P. Experimental and numerical study of cavitation inception phenomenon in diesel injector nozzles. International Communications in Heat and Mass Transfer2015;65:117–24. Https://doi.org/10.1016/j.icheatmasstransfer.2015.04.009.

[62] Ghiji M., Goldsworthy L., Brandner P.A., Garaniya V., Hield P. Numerical and experimental investigation of early stage diesel sprays. Fuel2016;175:274–86. Https://doi.org/10.1016/j.fuel.2016.02.040.

[63] Ghiji M., Goldsworthy L., Brandner P.A., Garaniya V., Hield P. Analysis of diesel spray dynamics using a compressible eulerian/VOF/LES model and microscopic shadowgraphy. Fuel2017;188:352–66. Https://doi.org/10.1016/j.fuel.2016.10.041.

[64] Salvador F.J., Jaramillo D., Romero J.V., Roselló M.D. Using a homogeneous equilibrium model for the study of the inner nozzle flow and cavitation pattern in convergent–divergent nozzles of diesel injectors. Journal of Computational and Applied Mathematics2017;309:630–41. Https://doi.org/10.1016/j.cam.2016.04.010.

[65] Pickett L.M., Genzale C.L., Bruneaux G., Malbec L.M., Hermant L., Christiansen C., et al. Comparison of diesel spray combustion in different high–temperature, high–pressure facilities. SAE Interation Journal of Engines2010;3:156–81. Https://doi.org/10.4271/2010-01-2106.

[66] Kastengren A.L., Tilocco F.Z., Powell C.F., Manin J., Pickett L.M., Payri R., et al. Engine combustion network (ecn): Measurements of nozzle geometry and hydraulic behavior. Atomization and Sprays2012;22(12):1011–52. Https://doi.org/10.1615/AtomizSpr.2013006309.